A&A 471, 813–824 (2007)
DOI: 10.1051/0004-6361:20066361

Astronomy & Astrophysics

Near-infrared study of southern massive star formation regions

The case of IRAS 16571-4029 source

A. Roman-Lopes⋆

Resident Astronomer at Southern Astrophysical Research (SOAR) Telescope, Casilla 603, La Serena, Chile
e-mail: aroman@ctio.noao.edu

Received 7 September 2006 / Accepted 8 May 2007

ABSTRACT

Context. We present the results of a near-infrared survey of the young stellar cluster associated with the IRAS 16571-4029 source.
Aims. The main purpose of this survey is to study the cluster members and find the ionizing sources of the associated HII region.
Methods. The stellar population was studied by using color–color and color–magnitude diagrams, as well as by analysing the spectral energy distributions in the near- and mid-infrared wavelengths. The extended emission was studied by the construction of contour diagrams, which were compared with near- and mid-infrared images. We computed the corresponding number of Lyman continuum photons (using the integrated Brγ flux density) and compared it with that obtained from the 5 GHz flux density to derive a mean visual extinction.
Results. NIR observations in the direction of RCW116B reveal the presence of a young cluster of massive stars coincident with the IRAS 16571-4029 source. These observations, together with published radio data, MSX, and Spitzer images were used to determine some of the physical parameters of the region.
We found 102 cluster member candidates in an area of about 3×3 square arcmin, the majority of them showing excess emission in the NIR.
We found that IRAS 16571-4029 is formed by multiple infrared sources, all but one are associated with small groups of stars. This suggests that the fragmentation of massive molecular clouds generates the massive sub-clusters.
We derived a mean visual extinction of $A_V = 12.8\pm^{4.7}_{3.2}$. This result is independent of the assumed distance and agrees with the mean visual extinction $A_V = 14.4$, as obtained by previous spectroscopic observations of two NIR sources in the direction of the IRAS 16571-4029 source.
We also compare the results obtained in this study with those obtained in previous papers in this series finding a very good correlation between the number of cluster members N_s and the cluster radius r_c. The cluster radius varies from 0.2−0.3 pc (IRAS 15411-5352 and IRAS 16132-5039) until about 1 pc (IRAS 15408-5356).
The youngest clusters are those associated with the RCW95 complex (IRAS 15408-5356 and IRAS 15411-5353) with ages in the range $1.5-2 \times 10^6$ years, while the sources associated with the RCW106 (IRAS 16132-5039, IRAS 16177-5018) and RCW116B (IRAS 16571-4029) complexes have ages in the range $2.5-3 \times 10^6$ years. The oldest of them is the cluster associated with the RCW121 region (IRAS 17149-4029), which has an estimated age of 4.2×10^6 years.

Key words. ISM: HII regions – stars: pre-main sequence – Galaxy: structure

1. Introduction

Massive stars are formed inside dense molecular clouds and because they evolve very quickly, they can leave the main sequence still embedded in their parental molecular cloud. In fact, they are generally visible only during their early evolution at infrared wavelengths, although they can be detected indirectly through radio emission from the ultra-compact HII region they form. The work of Wood & Churchwell (1989), associating the colors of IRAS point sources with the presence of ultra compact HII regions, represented a starting point in the search for young and massive stellar clusters. On the other hand, the recent advent of highly sensitive near-infrared instrumentation enables us to develop direct studies of highly embedded galactic star formation regions. In this sense, the recently launched *Spitzer Space Telescope* has opened a new window onto the study of the birth sites of massive stars. Despite its modest size (0.85 m), the Spitzer Space Telescope is much more sensitive and has higher spatial resolution than previous infrared observatories (Werner et al. 2004). The combination of *J*, *H*, and *K* photometric studies with the IRAC data is a useful tool for investigating the nature of bright near- to mid-infrared sources, since it gives information about the stellar sources that could be powering them, expanding the wavelength coverage of the observed YSOs.

The southern HII region RCW 116B (IRAS 16571-4029) is a strong (11.7 Jy) and compact ($1.4' \times 1.3'$) 5 GHz source (PMNJ1700-4033), which was observed in the H109α and H110α recombination lines by Caswell & Haynes (1987). The CS (2−1) transition, typical of dense molecular clouds was detected by Bronfman et al. (1996), while Verma et al. (Verma et al. 2003) have mapped the region at two far infrared wavelengths (at 150 and 210 μm) with about 1 arcmin resolution, finding that the IRAS source is formed by multiple embedded sources. Bik et al. (2005) obtained high resolution *K*-band spectra of two stars in the region, concluding that their spectral types are compatible with O8V-B1V zero-age main sequence (ZAMS) stars. These facts, together with the presence of an IRAS source with

⋆ This research made use of data taken at Pico dos Dias Observatory – LNA/MCT – Brazil.

colors of compact HII regions (Woody & Churchwell 1989), indicate that massive star formation has recently occurred. The present paper is the last in a series (Roman-Lopes et al. 2003; Roman-Lopes & Abraham 2004a,b, 2006a,b) aimed at studying the stellar populations associated with IRAS sources that are known to have colors of ultra-compact HII regions (Wood & Churchwell 1989), and strong CS (2−1) emission (Bronfman et al. 1996). This work is organized as follows. In Sect. 2 we describe the observations and the data reduction procedures, in Sect. 3 we present our results, in Sect. 4 we compare the results obtained in this study with those obtained in previous papers, and in Sect. 5 we summarize the work.

2. Observations and data reduction

2.1. LNA near-infrared data

The NIR images were taken in the 2004 May observing run, using the Near Infrared Camera (CamIV) of the Laboratorio Nacional de Astrofisica, Brazil, which is based on a Hawaii 1024 × 1024 HgCdTe detector, attached to the 1.6 m Perkin-Elmer telescope. The observations were performed in the direction of IRAS 16571-4029 point source; we used the J and H broadband filters and the narrow K band filters centered on the continuum at 2.14 μm (C1) and on the Bracket gamma line at 2.17 μm (Brγ). The plate scale was 0.24 arcsec pixel^{-1}, and the mean values of full width at half maximum (*FWHM*) of the point-spread function (PSF), were 0.8, 0.9, and 0.95 arcsec at the J, H, and narrow band (nb) K images, respectively. The total integration time for the J and H bands were 420 and 300 s, respectively, and 1540 s for each of the narrow K band filters.

In order to subtract the background contribution, we took several frames in the direction of regions outside the IRAS source by dithering the telescope a few arc minutes apart from the IRAS coordinate. Sky frames were generated from a median-filtered set of the flattened frames in each band.

We obtained a set of dome flats, by taking several (typically 20) on and off frames at each filter, using an illuminated white spot in the telescope dome. The final flat-field frames were obtained by subtracting the off median combined frames from the on median combined frames. To produce a combined image from each set of frames, we aligned them using the IRAF subroutines, added the aligned frames, and trimmed the resulting image. We used DAOFIND to locate stars 3σ above the local background (in each band), and because of source confusion within the region, photometry was obtained using the PSF-fitting algorithm ALLSTAR in the DAOPHOT package (Stetson 1987). The zero-point photometric constants for each photometric band were derived by comparing 2MASS and instrumental CamIV magnitudes from a set of isolated stars in both the CamIV and 2MASS images, covering a wide range of magnitudes and colors (Roman-Lopes & Abraham 2006b). The final photometric errors were computed as the quadratic sum of the zero-point errors and the intrinsic uncertainty for each star as given by the ALLSTAR routine.

The values of the completeness limits for the J, H, and nbK (C1) bands are 17.2, 16.5, and 15.5 mag, respectively, and were derived from the point at which the number of detected sources of magnitude m, $N(m)$ deviates from a straight line in the log (N) versus m diagram, as can be seen in Fig. 1.

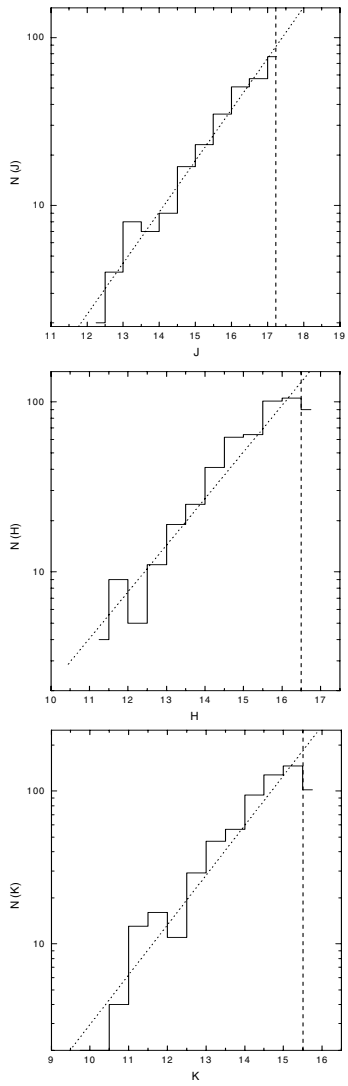

Fig. 1. The log (N) versus m diagram made from the J, H, and nbK CamIV magnitudes. The values of the completeness limits for the J, H, and nbK (C1) bands are 17.2, 16.5, and 15.5 mag, respectively, and were derived from the point at which the number of detected sources of magnitude m, $N(m)$ deviates from a straight line (indicated by the dashed line in each diagram).

2.2. IRAC-Spitzer data

The Infrared Array Camera (IRAC) of the Spitzer Space Telescope operates at four near- to mid-IR (MIR) bands centered at 3.6, 4.5, 5.8, and 8.0 μm. The images used in this work are sections of the original frames of the SIRTF Galactic Plane Survey. The IRAC Post-Basic Calibrated Data of the region around IRAS 16571-4029 were taken from the data archive of the Spitzer Science Center. Photometry of the Spitzer sources was obtained from the GLIMPSE Highly Reliable Catalog-version and also from the More Complete Archive Version[1]. Photometry of some prominent Spitzer sources not present in these catalog, was performed using the DAOPHOT package within IRAF, with an on-source aperture radius of 3 pixels and a sky annulus extending from 3 to 7 pixels. The aperture corrections and zero magnitude flux were applied following the procedure described in the Spitzer IRAC user manual.

[1] http://www.astro.wisc.edu/glimpsedata.html

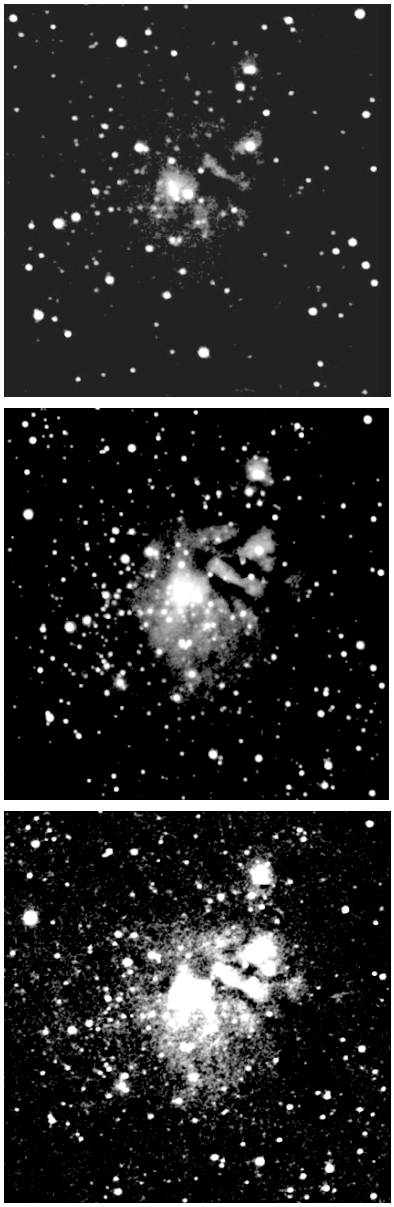

Fig. 2. *J* (*top*), *H* (*middle*), and *K* (C1) (*bottom*) infrared images (about 3.′4 × 3.′4). These images were taken using the NIR camera coupled to the 1.6 m Perkin-Elmer telescope, during the 2004 observing run. North is to the top, east to the left.

3. Results

In Fig. 2, we present the J, H, and *nbK* (C1) band images acquired during the 2004 May observing run. (top, middle, and bottom panels respectively).

3.1. The stellar cluster

As we can see from Fig. 2, the extinction in the direction of IRAS 16571-4029 might be highly variable. In fact, there are several obscured regions without a single IR source, suggesting the presence of dense molecular gas and dust. At the same time, some regions present a high number of bright infrared sources, as well as extended emission in the H and K bands. The large number of NIR sources that we can see mainly in the K band image suggest the existence of a stellar cluster still embedded in its parental molecular cloud. On the other hand, young clusters still enclosed in their parental molecular cloud frequently exhibit a high fraction of stars presenting excess emission at the NIR wavelengths.

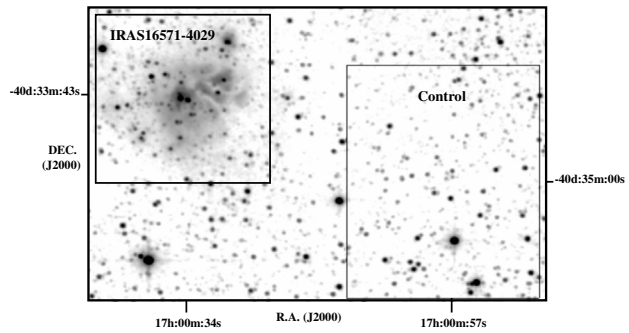

Fig. 3. The *K* band mosaic made with images taken from the interactive 2MASS image service. In this figure we show the IRAS 16571-4029 region (measuring about 3.4 × 3.4 square arcmin), which is centered at (J2000) 17h00m34 and −40d33m43s. On the right side, we indicate the location of the control region measuring about 6 × 4.6 square arcmin, which is centered at (J2000) 17h00m57s and −40d35m00s.

In order to address the question about the nature of the stellar population in the direction of the IRAS 16571-4029 source, we compared the NIR colors derived from our photometry with those obtained from the 2MASS catalog (excluding the sources weaker than the 2MASS completeness limits) for a selected nearby field labeled as *Control*, which probably consists of Galactic field stars. In Fig. 3, we present the *K* band mosaic made with the images taken from the interactive 2MASS image service[2]. There we show the IRAS 16571-4029 region (measuring about 3.4 × 3.4 square arcmin), which is centered at (J2000) 17h00m34 and −40d33m43s. On the right side of the same figure, we indicate the control region (measuring about 6 × 4.6 square arcmin), which is centered at (J2000) 17h00m57s and −40d35m00s.

We show in Fig. 4 the comparative color-color diagram constructed from the photometry of the IRAS 16571-4029 and control regions with the locus of the main-sequence and giant branch (Koornneef 1983) and the reddening vectors for early- and late-type stars (Fitzpatrick 1999). We can see from the control diagram two well defined groups separated by a gap around $J - H =$ 1.4. It is produced by the presence of the molecular cloud as inferred from the (2−1) CS emission observed by Bronfman et al. (1996). The first group is formed by foreground field stars, while the second is probably composed of reddened giant field stars; both groups lie inside the reddening band for the Galactic field population.

On the other hand, from the IRAS 16571-4029 color–color diagram, we note that a large number of NIR sources lie on the right side of the reddening band for the early-type stars. It is well known that during the early phase of the star formation process, young stellar objects (YSOs) are associated with circumstellar dust (Lada & Adams 1992), making them bright sources at infrared wavelengths since the dust absorbs and re-emits radiation from the embedded star. In this sense, the presence of a large number of sources showing excess emission at 2.2 μm indicates that the stellar population in the direction of the IRAS source must be very young.

By the study of the number of stars $N(J - H)$ and $N(H - K)$ as a function of the $(J - H)$ and $(H - K)$ colors, we obtained

[2] `http://irsa.ipac.caltech.edu/applications/2MASS/IM/interactive.html`

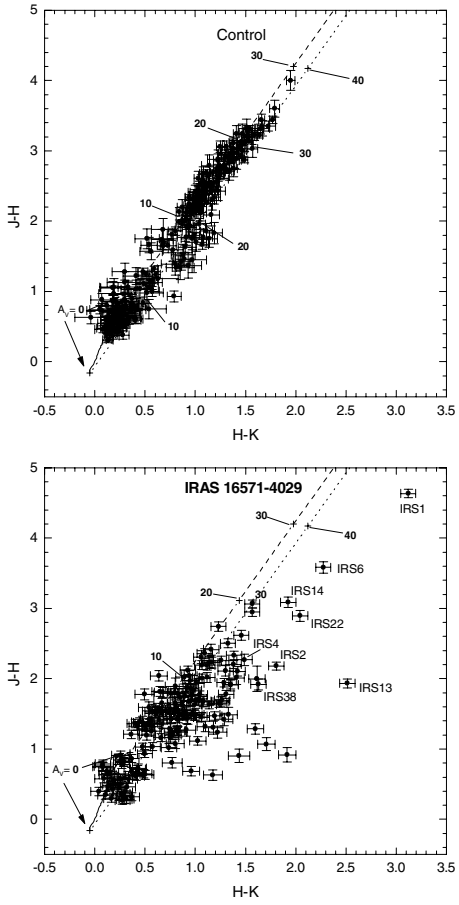

Fig. 4. The comparative color–color diagrams for the IRAS 16571-4029 and Control regions. The locus of the main sequence and the giant branch are represented by the solid lines (Koornneef 1983), while the reddening vectors for late- and early-type stars (Fitzpatrick 1999) are represented by the dashed and dotted lines, respectively.

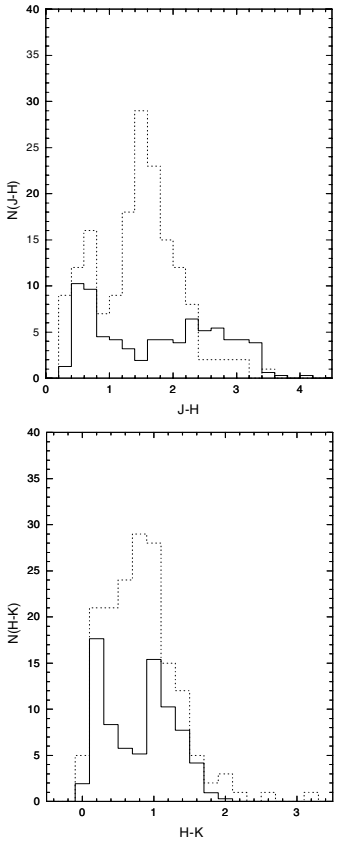

Fig. 5. The number of stars $N(J-H)$ and $N(H-K)$ as a function of the $(J-H)$ and $(H-K)$ colors from the control (solid lines) and IRAS 16571-4029 (dotted lines) areas. We can see that there is an excess of counts in the IRAS 16571-4029 region for sources presenting colors in the range $1.2 \leq (J-H) \leq 2.2$ and $0.3 \leq (H-K) \leq 1.1$.

additional constrains that enabled us to separate the cluster member candidates from the field stars. The results with the counts normalized to the area of the IRAS source region are shown in Fig. 5 where we can see that there is an excess of counts from the IRAS 16571-4029 source region for objects with colors in the range $1.2 \leq (J-H) \leq 2.2$ and $0.3 \leq (H-K) \leq 1.1$. In fact, from an inspection of the two diagrams, we observe that the maximum of the counts from the IRAS region coincides with the minimum of counts from the control region, suggesting that the majority of the NIR sources detected in the direction of the IRAS source, are probably members of the stellar cluster. Despite this last result, we must consider that an unknown fraction of the detected sources may come from Galactic field stars, so to minimize this effect, we used the following criteria to select the cluster member candidates:

1. NIR sources located in the IRAS source region and presenting excess emission in the $(J-H)$ versus $(H-K)$ diagram.
2. NIR sources located in the IRAS source region, lying along the reddening band for early-type stars, which have colors in the range $1.2 \leq (J-H) \leq 2.2$ and $0.3 \leq (H-K) \leq 1.1$.
3. NIR sources located in the IRAS source region not detected in the J band, which have colors in the range $0.3 \leq (H-K) \leq 1.1$ and also present bright IRAC counterparts.

The complete list of the selected NIR sources is shown in the table at the end of this article.

From Fig. 4 we can distinguish IRS1 and IRS6 as the reddest objects in the whole region. In fact, they present large near infrared colors forming together with the IRS2, IRS13, IRS14, and IRS22 sources, a group of very interesting objects. Unfortunately, there is no IRAC photometry for the IRS1 source, which appears saturated on the GLIMPSE images. This object will be discussed in some details in Sect. 3.4.

From the J versus $(J-H)$ diagram shown in Fig. 6, we can obtain additional information about the luminosity of the selected NIR sources. In that figure, we represent all sources detected at the J, H, and nbK bands with the locus of the main sequence corresponding to the kinematic distance of 1.1 kpc for $R_0 = 8.5$ kpc (Caswell & Haynes 1987) and the reddening vector for a B0 V star taken from Fitzpatrick (1999). As we could have already inferred from the IRAS 16571-4029 color–color diagram (Fig. 4), IRS1 is the brightest source in the whole region. The other bright NIR sources are IRS2, IRS4, IRS6, and IRS14, all exhibiting excess emission at 2.2 μm. We also note from Fig. 6 that there are several less luminous sources showing excess emission in the NIR. Some of these objects have bright *S pitzer* IRAC counterparts, making them good candidates for low-mass young stellar objects (Lada & Adams 1992).

On the other hand, there are a group of luminous stars (IRS3, IRS5, IRS7, IRS9, IRS10, IRS12, IRS17, and IRS21) that present $(J-H)$ colors in the range $0.75 \leq (J-H) \leq 1.5$, which do not show excess emission in the K band. The IRS3 source can be classified as a B0V main sequence star reddened by about 14 mag of visual extinction, while all the others may be

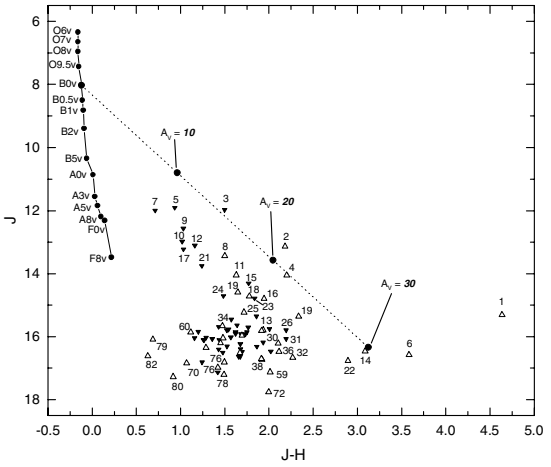

Fig. 6. The J versus $J-H$ diagram of the selected sources from Table 1. The locus of the main sequence at 1.1 kpc is shown by the solid line. The intrinsic colors are from Koornneef (1983), while the absolute J magnitudes were calculated from Hanson et al. (1997). The reddening vector for a B0V ZAMS star (*dotted line*) is from Fitspatrick (1999). We also indicate the location (*bold numbers*) of A_V = 10, 20, and 30 mag of visual extinction, as well as the sources that show excess emission (open triangles) and those that do not (filled triangles) in the color–color diagram.

Table 1. Integrated luminosity from the near- until the mid-infrared domain for the stronger MSX sources.

MSX ID	IRS	$L_{IR}(10^4\ L_\odot)$	Equiv. ZAMS Star
G345.2012+01.0562	1	3.3	O9.5V–B0V
G345.2028+01.0562	2, 3	3.1	O9.5V–B0V
G345.2124+01.0233	6, 7	6.5	O8.5V–O9V
G345.2244+01.0304	4, 8	3.1	O9.5V–B0V

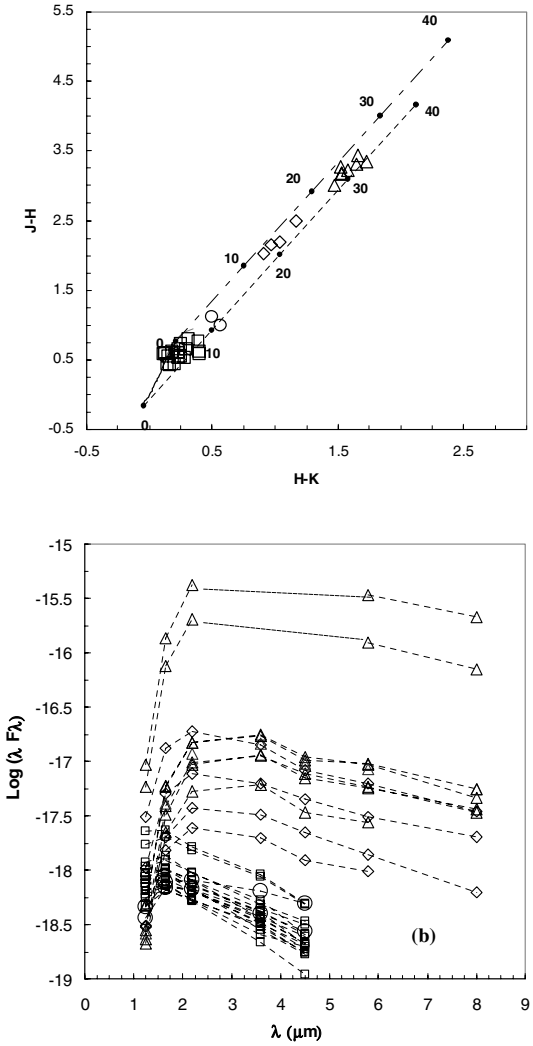

Fig. 7. a) The $J-H$ versus $H-K$ diagram from the Galactic field stars in the control region. **b)** The SED (between 1.25 μm and 8 μm) of the sources, constructed from the 2MASS and *Spitzer* IRAC photometric data. The symbols are as follow: squares represent the non-reddened or low-reddened field star, circles: the reddened main sequence stars, diamonds: the reddened giant stars and the triangles: highly reddened giant or super-giant stars.

classified as mid- to early-B main sequence stars, reddened by a mean visual extinction of 10 mag. Finally we observe that there are another group of less luminous stars (not showing excess emission at 2.2 μm) presenting $J-H$ mean values of about 1.6 mag and luminosity corresponding to A0V until F8V main-sequence stars.

3.2. Spectral energy distributions of the young IR sources

As we can see from Table 1, a large fraction of the selected NIR sources were detected by the IRAC survey and from the study of their NIR spectral energy distribution (SED) we can obtain additional constrains to classify and separate the cluster sources from the Galactic field population.

In order to compare the SEDs of the selected sources with that of field stars, we studied that from the control region. We used the data from the 2MASS and IRAC catalog, choosing sources covering a wide range of colors and reddening and, as result, obtained a sample as representative as possible of the Galactic field population. The corresponding $J-H$ versus $H-K$ diagram is shown in Fig. 7a, where we represented four types of sources:

1. non- and low-reddened main-sequence field stars;
2. reddened main-sequence field stars;
3. reddened giant field stars;
4. highly reddened giant and/or super-giant field stars;

In Fig. 7b we present the observed SED (between 1.25 μm and 8 μm) of the selected field stars. From that diagram we see that all SEDs of the highly reddened giant and/or super-giant field stars have maximum around 3.6 μm, decreasing slowly. On the other hand, the spectral energy distribution of the non- or low-reddened main sequence field stars have maxima around 2.2 μm, decreasing quickly at longer wavelengths.

In Fig. 8 we show the $J-H$ versus $H-K$ diagram of the selected sources in Table 1. There we represent only the sources detected in at least one of the IRAC bands (the exception is the IRS1 source). We can see that several of them lie along the reddening vector for hot stars. We refer to this group as *hot stars candidates* because they have luminosities (see Fig. 6) varying from B0 V (as is the case of the IRS3 source) until mid- and late-B main-sequence stars (IRS5, IRS7, IRS9, IRS12, IRS15, IRS21, and IRS33 sources). The observed SEDs of these group of sources are shown in Fig. 9.

Even though these sources do not appear to show excess emission in the K band, we note that the majority of them do

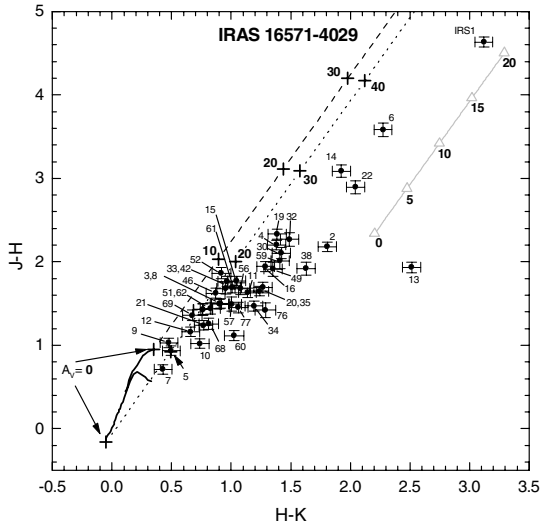

Fig. 8. The $J - H$ versus $H - K$ diagram of selected sources in Table 1. The locus of the main sequence and the giant branch are represented by the solid lines (Koornneef 1983), while the reddening vectors for late- and early-type stars (Fitzpatrick 1999) are represented by the dashed and dotted lines, respectively. We also show the position occupied by a modeled massive YSO (Whitney et al. 2004) powered by a B0V (light gray triangles) ZAMS star. We represent its $J - H$ and $H - K$ intrinsic colors reddened by 0, 5, 10, 15 and 20 mag of foreground extinction (Fitzpatrick 1999).

show some excess at longer wavelengths. In fact, all of them except IRS3, IRS10, IRS12, IRS33 and IRS69 exhibit SEDs characteristics of young stars surrounded by circumstellar disks. Further NIR spectroscopic studies will be necessary to clarify what fraction of these sources do show photospheric features and/or disk signatures.

In Fig. 10 we present the SEDs of the sources showing excess emission in the color–color diagram of Fig. 8. We have also constructed the SEDs from sources in Table 1 that were detected only in the H and K bands and that have a bright *S pitzer* IRAC counterpart. All of the SEDs are characteristic of young stellar objects. In fact, the sources detected in the direction of the IRAS region appear to cover wide range of masses, from luminous massive YSOs like IRS2, IRS6, IRS11, and IRS13 to the less luminous objects such as the IRS60, IRS87, IRS90, and IRS102 sources. In this sense, this cluster may become an excellent laboratory for testing the theory of formation and evolution of both, high-, and low-mass stars.

3.3. The IRAS source

As already mentioned, Verma et al. (2003) find that the IRAS 16571-4029 source is formed by multiple embedded sources. On the other hand, a more accurate position for the mid-infrared sources can be obtained from the Midcourse Space Experiment (*MSX*) Point Source Catalog[3]. *MSX* surveyed the entire Galactic plane within $| b | \leq 5$, in four mid-infrared spectral bands centered at 8.28, 12.13, 14.65, and 21.34 μm, with an image resolution of 19 arcsec and a global absolute astrometric accuracy of about 1.9 arcsec (Price et al. 2001).

In Fig. 11 we show the contour diagram constructed from the MSX *A*-band image (8.28 μm), overlaid on the LNA *K*-band image (*C*1 filter). From that figure we can see

[3] See `http://www.ipac.caltech.edu/ipac/msx/msx.html`

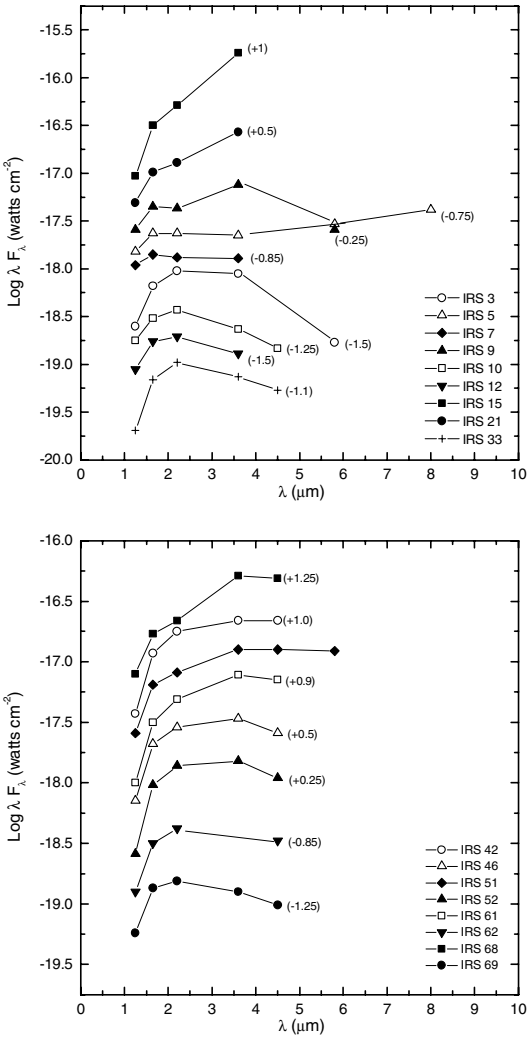

Fig. 9. The observed SED (between 1.25 μm and 8 μm) of the *hot stars candidates*. These stars do not show excess emission in the J, H, and K bands, but we can see that many of them do show some excess at longer wavelengths and may indicate the presence of disks. In order to clarify the presentation, the SEDs were shifted by the quantity shown to the right of them.

that the IRAS source is formed by at least seven components, which are indicated by the *MSX* identifiers. All the strongest sources (G345.2012+01.0562, G345.2028+01.0562, G345.2124+01.0233 and G345.2244+01.0304) have bright K band as well as *IRAC* counterparts. In that figure, we identify some of the near-infrared sources associated to the MSX sources by their respective identifiers, and also present separate details of the stars associated with the strongest MSX sources.

As we can see from Fig. 11, all but one of the strongest *MSX* sources have more than one NIR counterpart. This might indicate that each one of these IR sources are related with a subcluster, which suggest that the fragmentation of the large and massive molecular cloud originated the massive star clusters.

In Fig. 12 we present the near to mid-infrared SED of the strongest *MSX* sources, without any correction for absorption. The data were taken from the *LNA* survey (only in the case of the G345.2012+01.0562 source), and from the *IRAC* and *MSX* catalogs.

To obtain a rough estimate of the luminosity of the embedded NIR sources, we integrated the observed SEDs from the

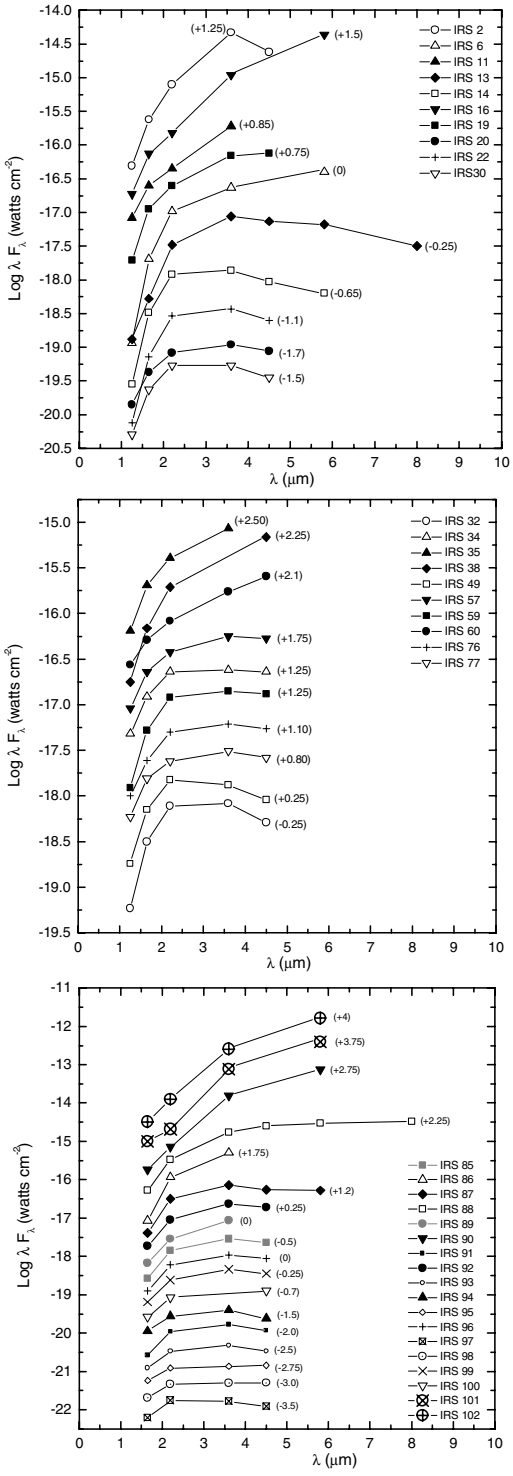

Fig. 10. The observed SED of selected sources presenting excess emission at 2 μm (upper and center). We also show the SEDs for objects detected only at the *H* and *K* LNA bands, which have a bright *IRAC* counterpart (down). In order to clarify the presentation, the SEDs were shifted by the quantity shown to their right.

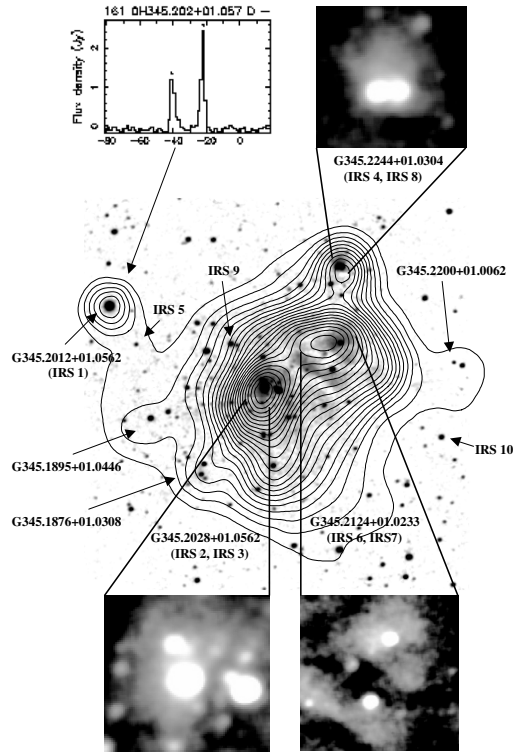

Fig. 11. The *nbK* band (*C*1) LNA image overlaid on the contour diagram made from the MSX *A* band image. We identify each of the MSX sources by labels; there are four prominent mid-infrared sources (G345.2012+01.0562, G345.2028+01.0562, G345.2124+01.0233 and G345.2244+01.0304), which have bright *K* band, as well as *IRAC* counterparts. We identify some of the *K* band near-infrared sources by their respective identifiers and also show a detailed vision of the stars associated to the stronger MSX sources. The double-peaked 1620 MHz OH maser (OH345.202+01.057), detected by Sevenster & Chapman (1997), associated to the IRS1 near-infrared source is shown in the upper-left corner of the figure.

near- to the mid-infrared domains, assuming a kinematic distance of 1.1 kpc. Considering the integrated infrared flux density as lower limits for the combined bolometric luminosity of the embedded stars, we derived their equivalent main-sequence spectral type, using the relation between spectral type and bolometric luminosity from Table 3 of the work of Hanson et al. (1997). The results are summarized in Table 2; the first column contain the MSX identifier while the associated main NIR sources are indicated in the second column. The last column contain the equivalent single ZAMS star, derived from the work of Hanson et al. (1997).

3.4. Brγ emission from the infrared nebula

In order to determine the contribution of the Brγ line emission to the observed extended emission, we scaled the Brγ to the continuum image (C1 filter) using the common bright field stars. Next we constructed the flux-calibrated contour diagram of the difference between the two images; and by measuring the area between contours, we computed the net Brγ flux density using the relation between magnitude and flux density given by Koornneef (1983), obtaining $F_{\mathrm{Br}\gamma} = (1.04 \pm 0.42) \times 10^{-10}$ erg cm^{-2} s^{-1}.

In Fig. 13, we show the 2.2 μm (LNA), 3.6 μm, and 5.8 μm (IRAC) images of the region toward these sources. In that figure we also present the 5.8 μm image overlaid by the continuum subtracted Brγ contour diagram. We found Brγ emission only in the direction of the G345.2028+01.0562 (IRS2-IRS3) and G345.2124+01.0233 (IRS6-IRS7) *MSX* sources. We can see that the Brγ emission comes from a small region, suggesting that the related HII region is very compact. In fact, the region where the Brγ emission is stronger has an angular diameter of about 15 arcsec, which corresponds to 0.08 parsec at the assumed distance of 1.1 kpc. On the other hand, the Brγ extended

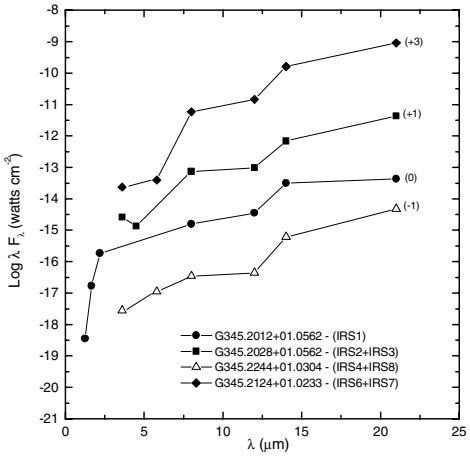

Fig. 12. The SEDs constructed from the near- to mid-infrared observed flux densities, for the G345.2012+01.0562, G345.2028+01.0562, G345.2124+01.0233, and G345.2244+01.0304 *MSX* sources. The data were taken from the LNA photometry (only for the G345.2012+01.0562 source) and from the *IRAC* and *MSX* catalog. Each one of this *MSX* sources are related with NIR counterparts, which are indicated by the black labels. For clarity the observed SEDs where shift by the quantity shown to the right of the last data point.

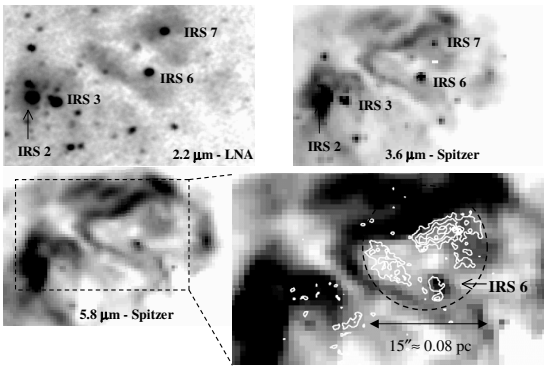

Fig. 13. The *C*1 (CamIV-*upper-left*), 3.6 μm (IRAC-*upper-right*) and 5.8 μm (IRAC-*lower-left*) images of the region associated with the Brγ emission. There we indicate the objects corresponding to IRS2, IRS3, IRS6, and IRS7 near-infrared sources. We also present the Brγ contour diagram (white lines), overlaying the 5.8 μm IRAC image (*lower-right*). We also indicate the approximated angular size (15 arcsec) of the Brγ region.

emission seems enclosed by the 5.8 μm dust emission. We also note in Fig. 13 that at the position of the IRS6 object, there is a strong 5.8 μm source that has an associated small Brγ extended emission.

To confirm the Brγ line emission from the IRS6 source, we performed point spread-function photometry in all sources present in the Brγ and *C*1 images. In Fig. 14, we present the difference between the derived magnitudes in both frames (Brγ-*C*1) as a function of the *K* magnitudes, for sources brighter than $K = 12$. We can see that two sources (IRS1 and IRS6) present a residual from the difference of the two *nbK* band photometry, which are larger than the quoted photometric uncertainty. We note that these two objects are just the reddest sources in the color–color diagram shown in Fig. 8, lying to the right side of the reddening vector for early-type stars. In this sense, the presence of strong Brγ point sources (line emission), may indicate the existence of very compact HII regions.

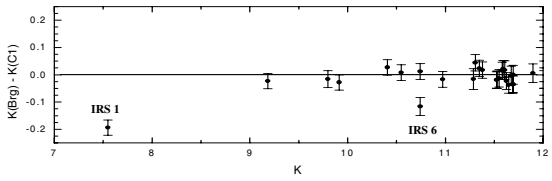

Fig. 14. The K(Brγ)-K(C1) versus K magnitude diagram, constructed from the PSF photometry of the common bright stars ($K \leq 12$). The anomalous sources in this diagram correspond to IRS1 and IRS6 sources (see text).

This result is particularly interesting in the case of the IRS1 source, which is the near-infrared counterpart of the G345.2012+01.0562 MSX source (see Fig. 11). It appears as a highly reddened object in the color–color diagram (see Fig. 4). We calculated the Brγ flux density associated to this object and found $S_{\mathrm{Br}\gamma} = (4.08 \pm 1.13) \times 10^{-11}$ erg cm^{-2} s^{-1}, which corresponds to about 40% of the measured flux density from the extended region. We note that this flux density comes from a very small region, which has a maximum diameter of 1 arcsec, which corresponds to the value of the *FWHM* of the point spread function associated to the IRS1 source, or about 0.005 pc at the quoted distance of 1.1 kpc. On the other hand, Sevenster & Chapman (1997) detected a double-peaked 1620 MHz OH maser (OH345.202+01.057, shown in Fig. 11), which can indicate the presence of expanding (or infalling) motions of material inside the region. High-resolution radio observation would be useful for clarifying the nature of this source.

Whitney et al. (2004) modeled the SEDs (from the near- to mid-infrared wavelengths) of highly embedded YSOs in star forming regions. They combined new *Spitzer* IRAC observations, together with the data from the 2MASS and the MSX surveys and found that some of the studied YSOs probably are powered by young O/B stars. Using the results from Fig. 6 of Whitney et al. (2004), we indicate in Fig. 8 the position of a massive YSO powered by a B0V central source. There we represented its $J-H$ and $H-K$ intrinsic colors reddened by 0, 5, 10, 15, and 20 mag of foreground extinction (Fitzpatrick 1999). By comparing these colors with those of the IRS1 source, we can do a rough estimate for the luminosity and also for the foreground extinction of this object. In this sense, the IRS1 source would be a YSO powered by a single B0V main sequence star, suffering a foreground extinction of about $A_{\mathrm{V}} = 20$ mag. We note that the inferred spectral type is compatible with the lower limit for the bolometric luminosity, which was obtained from the integral of the SED for the G345.2012+01.0562 MSX source (see Table 2).

3.5. Mean visual extinction and emission measure determined from the Brγ and radio flux densities

To estimate the mean visual extinction A_{V} in the direction of the nebula, we used the integrated Brγ flux density (uncorrected for reddening) to compute the corresponding number of Lyman continuum photons, using the expression derived by Ho et al. (1990):

$$N_{\mathrm{Ly}} = 2.9 \times 10^{45} \left(\frac{D}{\mathrm{kpc}}\right)^2 \left(\frac{3 S_{\mathrm{Br}\gamma}}{10^{-12}\ \mathrm{erg\ cm^{-2}\ s^{-1}}}\right) \mathrm{s}^{-1}. \quad (1)$$

We obtained $(3.6 \pm 1.4) \times 10^{47}$ photons s^{-1}. We can compare this result with that derived from the 6 cm flux density using the relation from Armand et al. (1996):

$$N_{\mathrm{Ly}}(6\ \mathrm{cm}) = 5.25 \times 10^{48} \left(\frac{D}{\mathrm{kpc}}\right)^2 T^{-0.45} S_{5\ \mathrm{GHz}}\ (\mathrm{Jy})\ \mathrm{s}^{-1}. \quad (2)$$

Table 2. Summary of derived parameters for the studied clusters.

Cluster	l	b	z^a	$N_{\rm star}{}^b$	$N_{\rm exc}{}^c$	f^d	$r_{\rm c}{}^e$	$A_{\rm V}{}^f$	$N_{\rm Ly}$(stars)^g	$N_{\rm Ly}$(radio)^h	$M_{\rm c}{}^i$	$r_{\rm d}{}^j$
IRAS 15408-5356	326.655	0.592	+24.8	136	96	70	0.98	12	1×10^{50}	3×10^{49}	1600	0.60
IRAS 15411-5352	326.726	0.613	+25.7	20	15	75	0.26	14–20	2×10^{48}	2.5×10^{48}	770	0.46
IRAS 16132-5039A	332.541	–0.128	–8.3	30	17	57	0.59	14	1.7×10^{49}	6×10^{48}	630	0.67
IRAS 16132-5039B	332.541	–0.128	–8.3	5	3	60	0.23	10	1.5×10^{47}	–	–	–
IRAS 16177-5018	333.306	–0.364	–21.6	41	24	58	0.60	28	1.6×10^{50}	5.2×10^{49}	4000	0.53
IRAS 16571-4029	345.208	+1.028	+19.73	102	55	55	0.54	12.8	1.4×10^{48}	1.3×10^{48}	500	0.62
IRAS 17149-3916	348.236	–0.976	–27.25	96	27	28	0.58	6.5	2.3×10^{49}	5.3×10^{48}	–	–

[a] Height scale (parsec). [b] Number of cluster member candidates. [c] Number of stars showing excess emission in the NIR. [d] Percentage of excess emission sources. [e] Estimated cluster radius (parsec). [f] Average visual extinction. [g] Total of Lyman continuum photons estimated from the massive cluster members. [h] Total of Lyman continuum photons derived from the 5GHz flux density (Caswell & Haynes 1987). [i] Total mass (solar masses) of the parental molecular cloud (Faundez et al. 2004). [j] Radius (parsec) of the core of the parental molecular cloud associated to the cluster (Faundez et al. 2004).

Assuming that the radio emission originates in the nebula and considering $T_{\rm e} = 7500$ K and $S_{5\ \rm GHz} = 11.7$ Jy (PMNJ1700-4033), we found $N_{\rm Ly}(6\ {\rm cm}) = 1.34 \times 10^{48}$ photons s^{-1}, which corresponds to a mean visual extinction $A_{\rm V} = 12.8\pm^{4.7}_{3.2}$ mag. This result (independent of the assumed distance) agrees with the mean visual extinction $A_{\rm V} = 14.4$, obtained by Bik et al. (2005) from spectroscopic observations of two NIR sources in the direction of the IRAS 16571-4029. It is interesting to note that the IRS3 source (located close to the Brγ extended emission) appears reddened by about 14 mag in the V band (see the color–magnitude diagram shown in Fig. 6), which is the same amount of extinction mentioned above.

We calculate the emission measure E from the detected 5 GHz flux density, using the observed size of the Brγ extended emission (about 15 arcsec) and the expression for the expected free-free emission from an optically thin plasma at wavelength λ, which is given by

$$S_\nu = 5.4 \times 10^{-16} g_{\rm ff}(\lambda, T) \Omega E T^{-1/2} {\rm e}^{-hc/\lambda kT}\ {\rm Jy}, \quad (3)$$

where E is the emission measure (cm^{-5}), Ω the solid angle of the source, and $g_{\rm ff}(\lambda, T)$ the Gaunt factor, which for radio wavelengths can be calculated from

$$g_{\rm ff}(\lambda, T) = \frac{\sqrt{3}}{\pi}\left[17.7 + \ln\left(\frac{T^{3/2}\lambda}{c}\right)\right]. \quad (4)$$

Assuming $T = 7500$ K, $L = 0.08$ pc, and $S_\nu = 11.7$ Jy, we found $E = 9.4 \times 10^{25}$ cm^{-5}, which results in a mean electron density $n_{\rm e} = 1.95 \times 10^4$ cm^{-3}, characteristic of ultra-compact HII regions (Churchwell 2002).

4. Comparison with other clusters in this series

As mentioned before, this work is part of a survey aimed at studying the stellar populations associated with IRAS sources, which have the colors of compact HII regions (Wood & Churchwell 1989) and intense CS (2−1) emission (Bronfman et al. 1996). In this sense, it is interesting to compare the results found in this study with those from the other papers. In Table 2, we present a summary of the main results from this work and from the other articles in this series. In Cols. 1–3 we indicate the IRAS identifiers and the Galactic coordinates. In Col. 4 we can see the corresponding height scale (the cluster distance measured from the galactic plane), in Col. 5 we show the number of cluster members, in Cols. 6 and 7 we tabulate the number of sources presenting NIR excess emission, and the corresponding measured fraction. In Col. 8 we indicate the estimated cluster radius, in Col. 9 the mean visual extinction, and in Cols. 10 and 11, we present the number of Lyman continuum photons, which were inferred from the most massive stars in each cluster and from the 5 GHz radio flux densities (Caswell & Haynes 1987), respectively. Finally in Cols. 12 and 13, we show the values for the mass of the associated parental molecular cloud and the values for the cloud core radius (Faundez et al. 2004).

4.1. Discussion

It is now generally accepted that most stars form in clusters (Lada & Lada 1995); but quantitative estimates of the fraction of stars that form in both, large and small clusters, groups and in relative isolation, is still an open issue. Following this hint, the observational parameters like the fraction of star presenting infrared excess in a given cluster, the relative ages of the clusters inside a given molecular cloud, the total number of stars formed in a given star forming region, the present-day mass function, etc, provides the fundamental clues to the development of the theory of star formation, in both the low- and high-mass regimes.

In a recent work, Adams and co-workers (Adams et al. 2006) found a correlation between the number of stars in a cluster ($N_{\rm s}$) and the cluster radius ($r_{\rm c}$). They argue that the average surface density of cluster members is almost constant, varying by less than an order of magnitude. This result was obtained for a sample of clusters within 1 kpc from the Sun. We can check this relation for more distant clusters using our results for $N_{\rm s}$ and $r_{\rm c}$, noting that all of the studied clusters have distances greater than 1 kpc from the Sun. Using the values presented in Table 3 (Cols. 5 and 8), we plotted the observed relation between $N_{\rm s}$ and $r_{\rm c}$ in Fig. 15. In that figure, we also represented the lines of constant column density using the values from Fig. 6 of Adams et al. (2006), which delineate the range where the correlation is valid. We can see a very close correlation between $N_{\rm s}$ and $r_{\rm c}$, and despite the small number of clusters in our sample, this result suggests that deeply embedded and distant massive young stellar clusters also follow the Adams relation.

Another important cluster parameter, is that related with the frequency of cluster members that show NIR excess emission due to the presence of disks. The initial disk frequency (IDF) and the variation of the cluster-disk frequency (CDF) with the cluster age, sets the timescale for both, the disk evolution and the lifetime of the circunstellar disk phase (Lada & Lada 2003). Haisch et al. (2001) performed a systematic observational survey for circumstellar disks in young clusters, and they found that

Table 3. List of selected NIR sources.

IRS	RA (J2000)	Dec (J2000)	J	H	K	3.6 μm	4.5 μm	5.8 μm	8 μm
1	255.1125	−40.54586	15.32 ± 0.05	10.68 ± 0.03	7.56 ± 0.07				
2	255.1411	−40.56058	13.14 ± 0.05	10.96 ± 0.03	9.15 ± 0.07	6.26 ± 0.22	6.49 ± 0.20		
3	255.1438	−40.56117	11.98 ± 0.05	10.48 ± 0.03	9.58 ± 0.07	8.69 ± 0.11			
4	255.1579	−40.54386	14.06 ± 0.05	11.86 ± 0.03	10.48 ± 0.07	6.21 ± 0.09		3.72 ± 0.09	
5	255.1180	−40.56328	11.91 ± 0.04	10.98 ± 0.03	10.48 ± 0.07			8.59 ± 0.12	6.95 ± 0.14
6	255.1547	−40.55896	16.59 ± 0.08	13.00 ± 0.03	10.73 ± 0.07	8.89 ± 0.10		7.34 ± 0.09	
7	255.1569	−40.55513	12.00 ± 0.05	11.29 ± 0.03	10.86 ± 0.07	9.91 ± 0.22			
8	255.1588	−40.54390	13.44 ± 0.05	11.94 ± 0.03	11.03 ± 0.07	6.21 ± 0.09		3.72 ± 0.09	
9	255.1354	−40.55347	12.57 ± 0.05	11.54 ± 0.03	11.07 ± 0.07				
10	255.1745	−40.57096	12.98 ± 0.05	11.96 ± 0.03	11.22 ± 0.07	10.77 ± 0.07	10.79 ± 0.12		
11	255.1802	−40.56049	14.05 ± 0.05	12.42 ± 0.03	11.28 ± 0.07	8.75 ± 0.09			
12	255.1562	−40.54625	13.11 ± 0.05	11.95 ± 0.03	11.28 ± 0.07				
13	255.1293	−40.53744	15.79 ± 0.05	13.86 ± 0.03	11.35 ± 0.07	9.34 ± 0.08	9.02 ± 0.05	8.66 ± 0.11	8.49 ± 0.13
14	255.1669	−40.57748	16.47 ± 0.06	13.38 ± 0.03	11.46 ± 0.07	10.34 ± 0.09	10.29 ± 0.09	10.22 ± 0.23	
15	255.1414	−40.55595	14.31 ± 0.05	12.53 ± 0.03	11.49 ± 0.07				
16	255.1410	−40.57242	14.80 ± 0.05	12.85 ± 0.03	11.57 ± 0.07	8.47 ± 0.12		6.00 ± 0.10	
17	255.1267	−40.57248	13.22 ± 0.05	12.19 ± 0.03	11.61 ± 0.07				
18	255.1408	−40.55931	14.72 ± 0.05	12.95 ± 0.04	11.64 ± 0.07				
19	255.1451	−40.56545	15.37 ± 0.05	13.03 ± 0.03	11.65 ± 0.07	9.59 ± 0.32	9.00 ± 0.13		
20	255.1293	−40.54980	14.60 ± 0.05	12.96 ± 0.03	11.72 ± 0.07	10.46 ± 0.16	10.22 ± 0.10		
21	255.1375	−40.57568	13.76 ± 0.05	12.52 ± 0.03	11.75 ± 0.07				
22	255.1592	−40.57861	16.77 ± 0.07	13.88 ± 0.03	11.83 ± 0.07	10.64 ± 0.16	10.58 ± 0.09		
23	255.1398	−40.56755	14.79 ± 0.05	12.95 ± 0.04	11.97 ± 0.07				
24	255.1524	−40.56422	14.71 ± 0.05	13.23 ± 0.03	12.27 ± 0.07				
25	255.1462	−40.56230	15.23 ± 0.05	13.52 ± 0.03	12.48 ± 0.07				
26	255.1397	−40.56796	15.80 ± 0.05	13.60 ± 0.03	12.54 ± 0.07				
27	255.1462	−40.56542	15.81 ± 0.05	13.89 ± 0.03	12.54 ± 0.07				
28	255.1411	−40.56776	15.36 ± 0.05	13.50 ± 0.04	12.55 ± 0.07				
29	255.1370	−40.56266	15.76 ± 0.05	13.76 ± 0.03	12.69 ± 0.07				
30	255.1728	−40.57999	16.22 ± 0.06	14.11 ± 0.03	12.69 ± 0.07	11.73 ± 0.11	11.69 ± 0.09		
31	255.1341	−40.56230	16.07 ± 0.06	13.87 ± 0.03	12.76 ± 0.07				
32	255.1650	−40.57681	16.67 ± 0.07	14.40 ± 0.04	12.91 ± 0.07	11.89 ± 0.12	11.92 ± 0.10		
33	255.1233	−40.58618	15.71 ± 0.05	13.94 ± 0.03	12.97 ± 0.07	12.39 ± 0.14	12.25 ± 0.09		
34	255.1710	−40.56922	15.66 ± 0.05	14.19 ± 0.03	13.00 ± 0.07	11.99 ± 0.06	11.56 ± 0.08		
35	255.1279	−40.55947	15.96 ± 0.05	14.27 ± 0.03	13.00 ± 0.07	11.25 ± 0.21			
36	255.1497	−40.55862	16.47 ± 0.07	14.36 ± 0.03	13.06 ± 0.07				
37	255.1119	−40.57582	15.45 ± 0.05	13.88 ± 0.04	13.06 ± 0.07				
38	255.1164	−40.56886	16.73 ± 0.07	14.81 ± 0.03	13.18 ± 0.07		10.35 ± 0.20		
39	255.1376	−40.56385	15.64 ± 0.05	14.00 ± 0.04	13.20 ± 0.07				
40	255.1562	−40.53969	15.86 ± 0.06	14.11 ± 0.03	13.22 ± 0.07				
41	255.1426	−40.55424	16.18 ± 0.05	14.25 ± 0.03	13.24 ± 0.07				
42	255.1226	−40.57014	15.92 ± 0.06	14.24 ± 0.03	13.28 ± 0.07	12.10 ± 0.23	11.60 ± 0.14		
43	255.1238	−40.57373	15.91 ± 0.06	14.29 ± 0.03	13.30 ± 0.07				
44	255.1490	−40.55280	16.47 ± 0.06	14.45 ± 0.03	13.33 ± 0.07				
45	255.1557	−40.54831	15.92 ± 0.05	14.19 ± 0.03	13.33 ± 0.07				
46	255.1475	−40.53352	15.85 ± 0.05	14.23 ± 0.03	13.36 ± 0.07	12.24 ± 0.12	12.06 ± 0.12		
47	255.1478	−40.54642	15.80 ± 0.05	14.27 ± 0.04	13.38 ± 0.07				
48	255.1466	−40.57460	15.78 ± 0.05	14.23 ± 0.03	13.41 ± 0.07				
49	255.1661	−40.59164	16.70 ± 0.08	14.79 ± 0.04	13.44 ± 0.07	12.63 ± 0.16	12.55 ± 0.12		
50	255.1424	−40.55978	16.36 ± 0.06	15.07 ± 0.04	13.47 ± 0.07				
51	255.1203	−40.54147	15.69 ± 0.05	14.26 ± 0.04	13.50 ± 0.07	12.06 ± 0.13	11.58 ± 0.08	11.13 ± 0.32	
52	255.1240	−40.56906	16.32 ± 0.06	14.46 ± 0.04	13.54 ± 0.07	12.49 ± 0.17	12.36 ± 0.15		
53	255.1669	−40.57689	16.05 ± 0.06	14.57 ± 0.04	13.58 ± 0.07				
54	255.1536	−40.55647	16.51 ± 0.06	14.84 ± 0.04	13.58 ± 0.07				
55	255.1377	−40.56134	16.23 ± 0.06	14.56 ± 0.04	13.62 ± 0.07				
56	255.1355	−40.55711	16.39 ± 0.06	14.72 ± 0.04	13.64 ± 0.07	11.40 ± 0.30	10.92 ± 0.21		
57	255.1234	−40.55130	16.20 ± 0.06	14.75 ± 0.04	13.69 ± 0.07	12.32 ± 0.19	11.89 ± 0.15		
58	255.1533	−40.56619	16.02 ± 0.05	14.45 ± 0.03	13.70 ± 0.07				
59	255.1466	−40.53660	17.13 ± 0.09	15.12 ± 0.04	13.71 ± 0.07	12.57 ± 0.15	12.16 ± 0.11		

the disk fraction rapidly drops with cluster age. They conclude that for a one-million year cluster age, the disk fraction is about 80 percent, dropping to only 10 percent for a five million years cluster age. In this sense, the direct measurement of the cluster disk frequency (inferred from the fraction of sources showing excess emission) in young highly embedded clusters, enable us to estimate the cluster's age.

Table 3. continued.

IRS	RA (J2000)	Dec (J2000)	J	H	K	3.6 μm	4.5 μm	5.8 μm	8 μm
60	255.1284	−40.53779	15.87 ± 0.05	14.76 ± 0.04	13.73 ± 0.07	11.96 ± 0.19	11.05 ± 0.11		
61	255.1257	−40.55774	16.49 ± 0.06	14.79 ± 0.04	13.79 ± 0.07	12.35 ± 0.16	11.96 ± 0.16		
62	255.1148	−40.57414	16.11 ± 0.06	14.67 ± 0.03	13.84 ± 0.08		12.65 ± 0.11		
63	255.1502	−40.56462	15.85 ± 0.05	14.65 ± 0.04	13.87 ± 0.07				
64	255.1520	−40.53931	16.64 ± 0.07	14.97 ± 0.03	13.89 ± 0.07				
65	255.1294	−40.55603	16.31 ± 0.06	14.79 ± 0.04	14.00 ± 0.07				
66	255.1425	−40.56210	16.04 ± 0.06	14.75 ± 0.06	14.00 ± 0.08				
67	255.1588	−40.54669	16.11 ± 0.06	14.85 ± 0.04	14.03 ± 0.07				
68	255.1373	−40.54397	16.11 ± 0.06	14.85 ± 0.03	14.04 ± 0.07	12.16 ± 0.11	11.73 ± 0.10		
69	255.1387	−40.53946	16.08 ± 0.05	14.72 ± 0.03	14.04 ± 0.07	13.32 ± 0.23	13.11 ± 0.12		
70	255.1422	−40.55763	16.84 ± 0.08	15.77 ± 0.04	14.06 ± 0.08				
71	255.1461	−40.56756	16.05 ± 0.05	14.89 ± 0.04	14.14 ± 0.07				
72	255.1547	−40.54143	17.76 ± 0.17	15.76 ± 0.04	14.14 ± 0.07				
73	255.1519	−40.55077	16.51 ± 0.06	15.03 ± 0.04	14.15 ± 0.08				
74	255.1265	−40.57633	16.63 ± 0.07	14.98 ± 0.04	14.18 ± 0.07				
75	255.1162	−40.57464	16.40 ± 0.06	14.97 ± 0.03	14.21 ± 0.07	13.38 ± 0.13	13.09 ± 0.15		
76	255.1251	−40.57752	16.98 ± 0.08	15.56 ± 0.04	14.27 ± 0.08	13.08 ± 0.21	12.74 ± 0.12		
77	255.1406	−40.53545	16.81 ± 0.08	15.32 ± 0.04	14.31 ± 0.08	13.10 ± 0.11	12.79 ± 0.10		
78	255.1528	−40.56721	17.20 ± 0.10	15.71 ± 0.04	14.38 ± 0.08				
79	255.1657	−40.56205	16.09 ± 0.06	15.40 ± 0.04	14.44 ± 0.08				
80	255.1443	−40.57653	17.28 ± 0.09	16.36 ± 0.04	14.45 ± 0.08				
81	255.1636	−40.56302	16.81 ± 0.07	15.57 ± 0.04	14.74 ± 0.08				
82	255.1515	−40.57753	16.62 ± 0.07	15.99 ± 0.04	14.81 ± 0.09				
83	255.1403	−40.57414	17.13 ± 0.11	15.71 ± 0.04	14.89 ± 0.10				
84	255.1536	−40.55650	16.51 ± 0.06	14.84 ± 0.04	13.58 ± 0.07				
85	255.1275	−40.57101		13.98 ± 0.03	11.49 ± 0.07	9.76 ± 0.28	9.50 ± 0.15		5.82 ± 0.14
86	255.1502	−40.54590		13.99 ± 0.03	11.65 ± 0.07	9.90 ± 0.12	9.67 ± 0.07		
87	255.1572	−40.56420		15.83 ± 0.04	12.49 ± 0.07	9.94 ± 0.17			
88	255.1564	−40.58316		15.27 ± 0.04	12.52 ± 0.07	10.66 ± 0.09	10.48 ± 0.07	10.05 ± 0.17	
89	255.1316	−40.57752		15.11 ± 0.04	12.61 ± 0.07	9.83 ± 0.11	8.92 ± 0.07	8.29 ± 0.13	7.53 ± 0.21
90	255.1518	−40.57197		14.85 ± 0.04	12.75 ± 0.07	10.60 ± 0.16			
91	255.1273	−40.57316		15.02 ± 0.04	13.03 ± 0.07	8.71 ± 0.13		6.04 ± 0.10	
92	255.1402	−40.57889		15.20 ± 0.04	13.17 ± 0.07	11.74 ± 0.26	11.64 ± 0.17		
93	255.1232	−40.56360		14.80 ± 0.03	13.18 ± 0.07	11.87 ± 0.19	11.75 ± 0.12		
94	255.1491	−40.58900		14.92 ± 0.04	13.42 ± 0.07	12.10 ± 0.18	12.12 ± 0.19		
95	255.1190	−40.57225		15.01 ± 0.04	13.68 ± 0.07	12.61 ± 0.23	12.05 ± 0.11		
96	255.1391	−40.58753		16.03 ± 0.04	13.82 ± 0.07	12.24 ± 0.13	11.95 ± 0.09		
97	255.1209	−40.58884		15.55 ± 0.04	13.89 ± 0.07	13.01 ± 0.15	12.86 ± 0.10		
98	255.1681	−40.53771		15.50 ± 0.04	14.09 ± 0.07	13.07 ± 0.12	12.55 ± 0.11		
99	255.1337	−40.58751		16.13 ± 0.04	14.18 ± 0.08	12.52 ± 0.20	12.34 ± 0.10		
100	255.1530	−40.54546		15.98 ± 0.04	14.21 ± 0.07		12.33 ± 0.21		
101	255.1290	−40.56987		15.66 ± 0.04	14.34 ± 0.08	9.49 ± 0.16		6.74 ± 0.11	
102	255.1273	−40.57315		15.02 ± 0.04	13.03 ± 0.07	8.78 ± 0.14		5.81 ± 0.07	

From the fraction of sources presenting excess emission (shown in Col. 7 of Table 3), we estimated the cluster age, using the results derived by Haisch et al. (2001). The youngest clusters are those associated with the RCW95 complex (IRAS 15408-5356 and IRAS 15411-5352) with ages in the range $1.5-2 \times 10^6$ years, while the sources associated with the RCW106 (IRAS 16132-5039, IRAS 16177-5018) and RCW116B (IRAS 16571-4029) complexes have ages in the range $2.5-3 \times 10^6$ years. The oldest of them is the cluster associated with the RCW121 region (IRAS 17149-4029), which has an estimated age of 4.2×10^6 years.

The mean visual extinction of the embedded stellar clusters is typically about 10−20 mag; however, it can be as high as 28 mag, as is the case of the IRAS 16177-5018 cluster. It is interesting to note that the oldest cluster in our sample (IRAS 17149-3916) is just who shows the small mean visual extinction (A_V = 6.5 mag). From Col. 8 of Table 3 we can see that the cluster radius varies from 0.2−0.3 pc (IRAS 15411-5352 and IRAS 16132-5039) to about 0.98 pc (IRAS 15408-5356). These results are compatible with those obtained from the study of the 1.2 mm continuum emission (Col. 12 of Table 3) of the associated molecular clouds (Faundez et al. 2004).

A comparison between the total mass of the associated cloud core and the estimated number of Lyman continuum photons (direct related to the number of massive stars in a given cluster) suggests that the more massive the cloud, the more massive (and numerous) the produced stars. This result seems to be obvious, but we need to show it in practice by the study of a large number of clusters and related parental molecular clouds. We also note that all of the studied clusters are confined in a narrow strip of the Galactic plane, which has a maximum height scale of ±30 pc.

5. Conclusions

NIR observations in the direction of the RCW116B complex reveal a young cluster of massive stars coincident with the

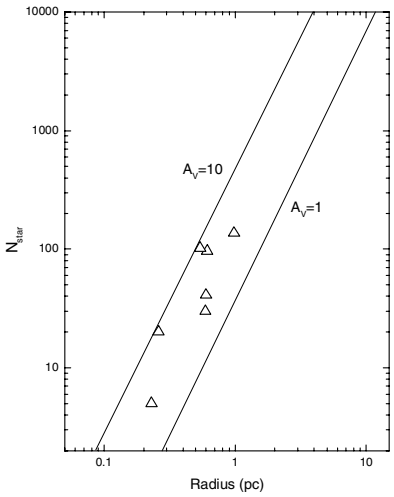

Fig. 15. The observed N_S versus cluster radius relation. The lines of constant column density for $A_V = 1$ and $A_V = 10$ were taken from the work of Adams et al. (2006).

IRAS 16571-4029 source. These observations, together with published radio data, MSX, and Spitzer images, were used to determine some of the physical parameters of the cluster.

We found 102 cluster member candidates in an area of about 3×3 square arcmin, the majority of them showing excess emission in the NIR. The strongest and reddest object in the region, IRS1 is associated with the G345.2012+01.0562 MSX source; it is also related to the double-peaked 1620 MHz OH345.202+01.057 maser. We found strong point source Brγ emission at the position of the IRS1 source, which indicates that this object can be a very young ultra-compact HII region. By comparing its infrared colors with the results obtained by models of massive YSOs, we found that IRS1 might be powered by a single B0V main sequence star.

We found that the IRAS 16571-5029 source is formed by multiple infrared sources, with all but one associated with small groups of stars. This suggests that the fragmentation of massive molecular clouds generates the massive sub-clusters.

From narrow band Brγ and continuum images we measured the extended Brγ flux density to obtain $F_{\mathrm{Br}\gamma} = 25 \pm 10$ mJy. Using the integrated Brγ flux density (uncorrected for reddening), we computed the corresponding number of Lyman continuum photons and compared it with what was obtained from the 5 GHz flux density to derive a mean visual extinction of $A_V = 12.8 \pm^{4.7}_{3.2}$. This result is independent of the assumed distance and agrees with the mean visual extinction $A_V = 14.4$, obtained by previous spectroscopic observations of two NIR sources in the direction of the IRAS 16571-4029 source.

From the observed size of the Brγ extended emission and the detected 5 GHz flux density, we calculated the emission measure $E = 9.4 \times 10^{25}$ cm^{-5} and electron density $n_e = 1.95 \times 10^4$ cm^{-3}, characteristic of ultra-compact HII regions (Churchwell 2002).

From a comparison between this cluster with others in this series we conclude that:

1. We have found a very good correlation between the number of cluster members N_s and the cluster radius r_c, and despite the limited number of clusters in our sample, this result suggest that deeply embedded and distant, massive young stellar clusters also follow the Adams relation.
2. From the fraction of sources showing excess emission, we estimated the age of the clusters, by using the results derived by Haisch et al. (2001). The youngest clusters are those associated with the RCW95 complex (IRAS 15408-5356 and IRAS 15411-5352) with ages in the range $1.5-2 \times 10^6$ years, while the sources associated with the RCW106 (IRAS 16132-5039, IRAS 16177-5018) and RCW116B (IRAS 16571-4029) complexes have ages in the range $2.5-3 \times 10^6$ years. The oldest of them is the cluster associated with the RCW121 region (IRAS 17149-4029), which has an estimated age of 4.2×10^6 years.
3. The mean visual extinction of the embedded stellar clusters is typically about 10−20 mag; however, it can be as high as 28 mag, as is the case of the IRAS 16177-5018 cluster.
4. The cluster radius varies from 0.2−0.3 pc (IRAS 15411-5352 and IRAS 16132-5039) to about 1 pc (IRAS 15408-5356). These results are compatible with those obtained from the study of the 1.2 mm continuum emission of the associated molecular clouds.
5. A comparison between the total mass of the associated cloud core and the estimated number of Lyman continuum photons (which is related to the number of massive stars in a given cluster) suggests that more massive the cloud, the more massive (and numerous) the produced stars.
6. All the massive clusters in our sample are confined to a tied region close to the Galactic plane in which the maximum height scale is ±30 pc.

Acknowledgements. This work was partially supported by the Brazilian agency FAPESP. We acknowledge the comments from the anonymous referee, which were valuable for improving the quality of the final manuscript. This publication makes use of data products from the Two Micron All Sky Survey, which is a joint project of the University of Massachusets and the Infrared Processing and Analysis Center/California Institute of Technology, funded by the National Aeronautics and Space Administration and the National Science Foundation. This research made use of data products from the Midcourse Space Experiment. This work is based [in part] on observations made with the Spitzer Space Telescope, which is operated by the Jet Propulsion Laboratory, California Institute of Technology under a contract with NASA.

References

Adams, F. C., Proszkow, E. M., Fatuzzo, M., & Myers, P. C. 2006, ApJ, in press [arXiv:astro-ph/0512330]
Armand, C., Baluteau, J.-P., Gry, C., & Cox, P. 1996, A&A, 306, 593
Bik, A., Kaper, L., Hanson, M. M., & Smiths, M. 2005, A&A, 440, 121
Bronfman, L., Nyman, L.-A., & May, J. 1996, A&A, 115, 81
Caswell, J. L., & Haynes, R. F. 1987, A&A, 171, 261
Churchwell, Ed. 2002, ARA&A, 40, 27
Faundez, S., Bronfman, L., Garay, G., et al. 2004, A&A, 426, 97
Fitzpatrick, E. L. 1999, PASP, 111, 63
Ho, Paul T. P., Beck, Sara C., & Turner, Jean L. 1990 ApJ, 349, 57
Hanson, M. M., Howarth, I. D., & Conti, P. S. 1997, ApJ, 489, 698
Koornneef, J. 1983, A&A, 128, 84
Lada, C. J., & Adams, F. C. 1992, ApJ, 393, 278
Lada, C. J., & Lada, E. A. 1995, AJ, 109, 1682
Lada, C. J., & Lada, E. A. 2003, ARA&A, 41, 57
Price, S. D., Egan, M. P., Carey, S. J., Mizuno, D. R., & Kuchar, T. A. 2001, AJ, 121, 2819
Roman-Lopes, A., & Abraham, Z. 2004a, AJ, 127, 2817
Roman-Lopes, A., & Abraham, Z. 2004b, AJ, 128, 2364
Roman-Lopes, A., & Abraham, Z. 2006a, AJ, 131, 951
Roman-Lopes, A., & Abraham, Z. 2006b, AJ, 131, 2223
Roman-Lopes, A., Abraham, Z., & Lépine, J. R. D. 2003, AJ, 126, 1896
Stetson, P. B. 1987, PASP, 99, 191
Sevenster, M. N., & Chapman, J. M. 1997, A&A, 122, 79
Verma, R. P., Ghosh, S. K., Kulkarni, V. K., & Ojha, D. K. 2003, Bull. Astron. Soc. India, 31, 399
Werner, M. W., et al. 2004, ApJS, 154, 1
Whitney, B., Indebetouw, R., Meade, M. R., et al. 2004, ApJS, 154, 315
Wood, D. O. S., & Churchwell, E. 1989, ApJ, 340, 265